



Cite this: *Dalton Trans.*, 2016, **45**, 15621

Synthesis, characterization, and water adsorption properties of a novel multi-walled carbon nanotube/MIL-100(Fe) composite†

Najam U. Qadir,^a Syed A. M. Said,^{*a,b} Rached B. Mansour,^{a,b} Khalid Mezghani^b and Anwar Ul-Hamid^c

Conventional small-scale adsorption chillers generally employ silica-gel/water or zeolite/water working pairs given the relatively high level of mesoporosity and water affinity in these adsorbent materials. However, the coefficient of performance (COP) and specific cooling power (SCP) evaluated for the adsorption chiller using these adsorbent/adsorbate pairs cannot be still considered practically feasible in the context of a commercial system. Metal organic frameworks (MOFs) are not only characterized by much higher water adsorption capacities than these materials, but also can be mass-produced using much simpler methods than the template-assisted synthesis routes of most zeolites. However, the low intrinsic thermal conductivity of these materials limits their use as adsorbents in commercial-scale adsorption chillers. In this study, a novel composite composed of multi-walled carbon nanotubes (MWCNTs) incorporated in a MIL-100(Fe) framework has been synthesized using a molecular-level mixing process. The resulting composite, with varying volume fraction of MWCNTs, has been characterized for microstructure, degree of crystallinity, thermal stability, water sorption kinetics and hydrothermal cyclic stability for potential use as an adsorbent in commercial adsorption chillers.

Received 3rd July 2016,
Accepted 26th August 2016

DOI: 10.1039/c6dt02640k

www.rsc.org/dalton

Introduction

Currently available adsorption chillers in the marketplace employ either silica-gel/water or zeolite/water as working pairs. These conventional systems, however, suffer from four main problems which still remain unresolved: (a) lower COP and SCP values due to lower water adsorption capacity and lower thermal conductivity respectively, (b) intermittent mode of operation, (c) need for very high vacuum to accelerate the rate of refrigerant desorption, and (d) a very low efficiency-to-weight ratio.^{9–20} In other words, the currently available adsorption chillers are only able to meet small-scale refrigeration needs, and cannot be considered viable in the context of a commercial-scale adsorption refrigeration system. Hence, for adsorption cooling technology to successfully replace the electrical cooling technology in the coming decade, significant improvements concerning the design of the system

and/or the choice of the adsorbent/adsorbate pair are required.^{5–20} As the most important property of the refrigerant with regard to adsorption refrigeration is its specific evaporation enthalpy, water is preferred to other refrigerants like ethanol, methanol, acetone, and chloroform, owing to its highest specific evaporation enthalpy. In this context, numerous research attempts have been made to synthesize the most appropriate adsorbent for achieving a practically feasible performance of a commercial adsorption chiller using water as a refrigerant.^{5–20} Although a vast majority of these potential adsorbents are either silica-gel- or zeolite-based, none can be considered practically viable for use in a commercial-scale adsorption chiller owing to the lower coefficient of performance (COP) as well as specific cooling power (SCP) achievable using these traditional adsorbents.

Composite adsorbents incorporate second-phase materials which are characterized either by a noticeably higher adsorption capacity than the base adsorbent or possess significantly higher thermal conductivity, resulting in improved heat and/or mass transfer characteristics of the base adsorbent.^{1–4,45} A variety of research studies have recently focused on the development of composite adsorbents for adsorption cooling applications. An adsorbent composed of expanded natural graphite (ENG) impregnated with NaBr has been developed for use in a batch scale sorption system using ammonia as a refrigerant.¹

^aCenter of Research Excellence in Renewable Energy, King Fahd University of Petroleum and Minerals (KFUPM), Dhahran 31261, Kingdom of Saudi Arabia

^bKACST-TIC Center of Carbon Capture and Sequestration, KFUPM, Dhahran 31261, Kingdom of Saudi Arabia. E-mail: samsaid@kfupm.edu.sa

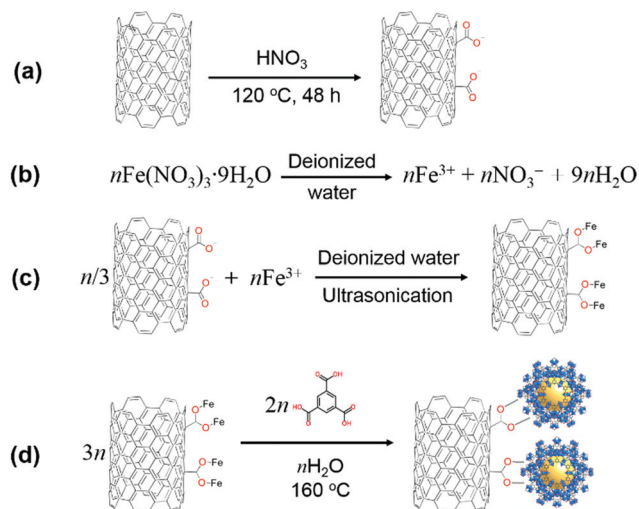
^cCenter of Engineering Research, KFUPM, Dhahran 31261, Kingdom of Saudi Arabia

†Electronic supplementary information (ESI) available. See DOI: 10.1039/c6dt02640k

Composite adsorbents have also been fabricated for an adsorption heat pump *via* impregnation of hydrophilic silica into the mesopores and micropores of activated carbons.² The water adsorption isotherms of the composite adsorbents were observed to shift to lower relative pressures, and the water adsorption capacity was found to be higher than those of raw activated carbons. In a similar manner, composite adsorbents involving varying volume fractions of ENG in activated carbon have also been developed for use in an adsorption refrigeration system.³ The heat transfer rate within the composite adsorbent was observed to increase to almost ten times that of activated carbon, while ammonia adsorption was found to increase by 29% at an evaporating temperature of 8 °C. More recently, a novel composite adsorbent comprising a hybrid sawdust/CaCl₂ matrix and ENG as the filler material has been fabricated for use in an adsorption chiller using ammonia as a refrigerant.⁴ The sawdust was carbonized and activated prior to composite fabrication in order to enhance the mass transfer characteristics of the adsorbent, while the heat transfer characteristics were improved by the addition of ENG. The composite adsorbent comprising 30 wt% ENG was evaluated to show the best performance for potential use in an adsorption chiller, resulting in an SCP of 801.7 W kg⁻¹ for an adsorption time of 10 min.

The abovementioned studies have incorporated second-phase materials in traditional adsorbents for achieving improved heat and/or mass transfer characteristics in order to accelerate the adsorption/desorption rates of the refrigerant and thus enhance the cooling efficiency of the adsorption chiller. However, in the context of the refrigeration demands of a commercial chiller application, the values of SCP and COP currently observed for the adsorption chiller using the resulting composite adsorbents still need further improvement. Since the filler material which is usually added for achieving better heat transfer characteristics is carbon-based and thus primarily hydrophobic, excessive filler addition is itself detrimental to the water adsorption characteristics of the base adsorbent. Hence, the only solution available to simultaneously improve the heat and mass transfer properties of the base adsorbent is the development of a base adsorbent with a preferably larger pore volume to accommodate a sufficient quantity of water molecules, even after the addition of an optimal quantity of filler material. In this context, metal organic frameworks (MOFs) are a class of micro/nanoporous materials which have been shown to possess water adsorption capacities much higher than those exhibited by their mesoporous counterparts like silica gels and zeolites.^{5–9} A number of recent research studies have focused on the use of MOFs as a potential adsorbent in adsorption chiller applications.^{7,10–20} However, due to the presence of an organic linker, which is present in a significantly greater proportion than metal ion centers, these materials still fail to have the heat transfer characteristics required of a commercially feasible adsorbent. A few recent research studies have focused on enhancing the thermal and/or electrical properties of MOFs either by incorporation of graphite-based materials like carbon nanotubes

(CNTs) or by producing thin MOF coatings on a metallic substrate.^{21–25} In this work, we have proposed a MOF, MIL-100(Fe), as a potential adsorbent for a commercial adsorption chiller using water as a refrigerant. MIL-100(Fe), based on μ_3 -oxo-centered trimers of Fe^{III} octahedra, is a crystalline three-dimensional iron(III) trimesate which possesses two types of mesoporous cages (25 and 29 Å), accessible windows (5 and 9 Å), excellent chemical and solvent stability, metal active sites and aromatic pore walls. The Brunauer–Emmett–Teller (BET) surface area and pore volume for this material have been measured to lie between 1500 and 2100 m² g⁻¹, and 0.65 and 1.2 cm³ g⁻¹ respectively, which combined with the aforementioned characteristics render it an excellent candidate for applications requiring cyclic adsorption/desorption of water molecules.^{7,8,34} It has been reported to show a maximum room temperature water vapour uptake of 0.65 g g⁻¹, coupled with an excellent hydrothermal cyclic stability, both of which are regarded as important pre-requisites for an adsorbent material to be used in a chiller application.^{7,8} In order to probe the effect of carbon on the adsorption behaviour and cyclic stability of this material, functionalized MWCNTs have been utilized as supports to grow the MIL-100(Fe) framework to form a chemically bound MWCNT/MIL-100(Fe) composite material (Scheme 1).^{26,27} Both MIL-100(Fe) and MWCNT/MIL-100(Fe) composites have been synthesized using similar procedures except for the addition of functionalized MWCNTs in varying amounts (60 mg, 180 mg, and 300 mg) during the *in situ* synthesis of the composite. The corresponding weight percentages of the added MWCNTs for each composite were measured to be 2.16, 5.90 and 10.72 respectively. The synthesized MWCNT/MIL-100(Fe) composites are referred to as **MC_n** with *n* from 1 to 3 corresponding to the amount of added MWCNTs



Scheme 1 (a) Chemical functionalization of MWCNT resulting in the attachment of negatively-charged carboxyl groups, (b) dissociation of precursor salt in aqueous medium, (c) sonication-assisted interaction of carboxyl groups on MWCNT with Fe³⁺ ions in aqueous medium, and (d) hydrothermal synthesis resulting in the growth of MIL-100(Fe) crystals on the MWCNT support with –C–O– groups acting as chemical hinges.

(60 mg, 180 mg and 300 mg respectively). The resulting MWCNT/MIL-100(Fe) composite, with varying volume fractions of MWCNTs, has been characterized for microstructure, degree of crystallinity, thermal stability, water sorption kinetics, and hydrothermal cyclic stability. The possibilities of using the proposed composite as a potential adsorbent in water-based adsorption chillers have been highlighted. Based on the results obtained from nitrogen and water adsorption isotherms, a critical weight fraction of MWCNTs results in the maximum achievable surface area and water vapour uptake, above which both these properties start to deteriorate owing to possible agglomeration of MWCNTs. The data obtained from water adsorption and cyclic stability tests indicate that a MWCNT content between 2 and 6 wt% in MIL-100(Fe) is recommended to achieve a reasonable compromise between water uptake and cyclic stability for successful use as an adsorbent in a commercial chiller application.

Experimental

Materials and general procedures

1,3,5-Benzenetricarboxylic acid (H_3 -BTC, $\geq 98\%$ purity), ferric nitrate nonahydrate ($Fe(NO_3)_3 \cdot 9H_2O$, $\geq 99\%$ purity), ammonium fluoride (NH_4F , 99.99% purity), and nitric acid (HNO_3 , 70% v/v) were purchased from Sigma Aldrich Chemical Co. Multi-walled carbon nanotubes (MWCNTs) were obtained from Cheap Tubes Inc. Both ethanol (99.999%) and deionized water were of highest purity available and used without further purification. All chemicals were used without further purification.

Powder X-ray diffraction (PXRD) analyses were performed using a Rigaku Ultima IV multipurpose diffractometer equipped with Ni-filtered $Cu K\alpha$ radiation. Samples were packed densely in a 0.5 mm deep well on a zero-background holder. Programmable divergence slits were used to illuminate a constant length of the samples (8 mm), thus preserving the constant volume assumption. The operating power of the diffractometer was set at 45 kV and 40 mA, and the diffraction data were collected between 3 and 50° (2θ) with a total scan time of 3 h. PXRD patterns for the residues recovered after thermogravimetric analysis, as well as the MOF samples subjected to cyclic water ad-/desorption tests, were recorded on a Bruker D8 Advance multipurpose diffractometer equipped with Ni-filtered $Cu K\alpha$ radiation. The operating power of the diffractometer was set at 35 kV and 25 mA, and the diffraction data were collected between 10 and 60° (2θ) with a step-size of 0.02046° and 0.25 s per step.

Fourier transform infrared (FTIR) spectra were recorded with KBr pellets on a Thermo Fisher Scientific Nicolet 6700 FTIR spectrometer. Output absorption bands are described as: s, strong; m, medium; w, weak; and br, broad. Scanning electron microscopy (SEM) and energy dispersive spectroscopy (EDS) were performed using a TESCAN LYRA3 FEG microscope. SEM samples were prepared by placing drops of the as-synthesized MOF suspended in acetone on Cu tapes. The

solvent was allowed to evaporate before the images were obtained at an accelerating voltage of 5 kV and a working distance of 5–6 mm with a standard secondary electron detector. X-ray photoelectron spectroscopy (XPS) measurements were conducted on a Thermo Scientific ESCALAB 250Xi X-ray photoelectron spectrometer. Transmission electron microscopy (TEM) was performed using a JEOL JEM-2100F/HR microscope. TEM samples were prepared by placing drops of the as-synthesized MOF suspended in ethanol on carbon-coated 200 mesh Cu grids. Images were collected using an accelerating voltage of 120 kV. Thermogravimetric analysis (TGA) was carried out using a TA Q500 thermal analyser under air flow with a heating rate of $5^\circ C min^{-1}$. Powdered samples were heated overnight at $120^\circ C$ to remove moisture prior to performing the TGA measurements. Elemental analysis (EA) was performed using high temperature combustion with a Perkin Elmer CHNS/O Series II 2400 Elemental Analyser.

Low-pressure nitrogen adsorption measurements were conducted using a Quantachrome Autosorb iQ volumetric gas sorption analyser. Ultrapure N_2 and He (99.999%) were used for all adsorption measurements. A liquid N_2 bath (77 K) was used in all N_2 isotherm measurements. The specific surface areas were evaluated using the BET method in the P/P_0 range of 0.06–0.2. The total pore volume was taken by a single-point method at $P/P_0 = 0.9$.

Heat capacity measurements were performed on a TA Q1000 modulated differential scanning calorimeter (MDSC) under nitrogen flow. All measurements were conducted using an aluminium hermetic sample pan with a heating rate of $10^\circ C min^{-1}$ and a gas flow rate of $50 ml min^{-1}$.

Functionalization of MWCNTs

Carboxylic acid-functionalized MWCNTs were prepared according to a reported procedure.²⁸ Specifically, MWCNTs (3 g) were first dispersed in 70% HNO_3 (200 mL) using sonication. The mixture was then transferred to a 250 mL round bottom flask equipped with a condenser and was refluxed at $120^\circ C$ for 48 h. After cooling to room temperature, the mixture was diluted with 500 mL deionized water and then vacuum filtered through a $2.5 \mu m$ polymeric membrane. The filtered powder was washed repeatedly with deionized water until the pH of the filtrate reached ~ 5.5 . The filtered powder was dried at $80^\circ C$ in air for 24 h and ground for further use. FT-IR (KBr , 4000 – $400 cm^{-1}$): 3883(w), 3768(w), 3444(s), 2956(w), 2929(m), 2855(w), 2662(br), 2357(w), 2082(br), 1775(w), 1500(w), 1290(m), 1097(br), 810(w), 670(w).

Synthesis of MIL-100(Fe)

The synthesis and activation of MIL-100(Fe) were carried out according to a previously reported procedure.³⁴ Briefly, $Fe(NO_3)_3 \cdot 9H_2O$ (4.04 g, 0.01 mol) was first dissolved in de-ionized water (50.2 mL, 2.8 mol) and the mixture was completely transferred to a 125 ml Teflon-liner containing BTC (1.4097 g, 0.00671 mol). The Teflon-liner was then sealed inside a stainless steel autoclave and kept at $160^\circ C$ for 14 h. The autoclave was cooled slowly to room temperature, after

which the “as-synthesized” dark orange solid was recovered using a centrifuge that was operated at 8000 rotations per min for 45 min. In order to remove any unreacted species, the as-synthesized MIL-100(Fe) was washed with copious amounts of water and ethanol and finally with an aqueous NH_4F solution. Specifically, the dried solid (1 g) was first immersed in de-ionized water (60 mL) and the resulting suspension was stirred at 70 °C for 5 h. The suspension was again centrifuged and the procedure was repeated using ethanol (60 mL) at 65 °C for 3 h. This two-step purification was continued until the decanted solvent following centrifugation became completely colourless, after which the solid was immersed in a 38 mM aqueous NH_4F solution and stirred at 70 °C for 5 h. The suspension was again centrifuged, after which the solid was washed 5 times with de-ionized water at 60 °C, and finally dried in air at 75 °C for 2 d followed by 95 °C for 2 d. FT-IR (KBr, 4000–400 cm^{-1}): 3494 (br), 2892(w), 1700(w), 1624(s), 1589(m), 1490(s), 1443(m), 1383(s), 1205(w), 1107(m), 1021(w), 937(m), 787(w), 757(s), 740(s), 708(s), 673(s), 575(s). EA (activated sample): Calcd for $\text{Fe}_3\text{O}(\text{H}_2\text{O})_2(\text{OH})(\text{NO}_3)_{0.12}[\text{C}_6\text{H}_3(\text{CO}_2)_3]_2 \cdot 28\text{H}_2\text{O}$: C, 18.59; H, 2.45; N, 0.14%. Found: C, 18.14; H, 2.70; N, 0.15%.

Synthesis of MWCNT/MIL-100(Fe) composites (MC1–3)

$\text{Fe}(\text{NO}_3)_3 \cdot 9\text{H}_2\text{O}$ (4.04 g, 0.01 mol) and a pre-determined amount of functionalized MWCNTs (60, 180 and 300 mg for **MC1**, **MC2** and **MC3**, respectively) were mixed thoroughly in the solid-state until a uniform colour of the mixture was achieved. Next, deionized water (5 mL) was then added periodically to the mixture and the resulting paste was sonicated until the water completely evaporated. The dry paste, along with BTC (1.4097 g, 0.00671 mol) and deionized water (50.2 mL, 2.8 mol), was then transferred completely to a 125 ml Teflon-lined autoclave, which was kept at 160 °C for 14 h. After allowing the reaction to cool to room temperature, the resulting solid was purified according to the same procedure previously employed for MIL-100(Fe). **MC1**: FT-IR (KBr, 4000–400 cm^{-1}): 3743(w), 3444(br), 2921(w), 2333(w), 2026(br), 1749(w), 1632(s), 1493(m), 1383(s), 1266(w), 1021(w), 836(w), 741(m), 674(w), 579(m). EA (activated sample): Calcd for $\text{Fe}_3\text{O}(\text{H}_2\text{O})_2(\text{OH})(\text{NO}_3)_{0.35}[\text{C}_6\text{H}_3(\text{CO}_2)_3]_2 \cdot 25\text{H}_2\text{O}$: C, 19.25; H, 1.90; N, 0.44%. Found: C, 18.96; H, 2.19; N, 0.47%. **MC2**: FT-IR (KBr, 4000–400 cm^{-1}): 3855(w), 3630(w), 3402(br), 2924(w), 2341(w), 2026(br), 1749(w), 1632(m), 1559(w), 1450(m), 1383(s), 1263(w), 1066(w), 860(w), 714(m), 572(w). EA (activated sample): Calcd for $\text{Fe}_3\text{O}(\text{H}_2\text{O})_2(\text{OH})(\text{NO}_3)_{0.3}[\text{C}_6\text{H}_3(\text{CO}_2)_3]_2 \cdot 15\text{H}_2\text{O}$: C, 23.01; H, 2.55; N, 0.45%. Found: C, 22.84; H, 2.18; N, 0.46%. **MC3**: FT-IR (KBr, 4000–400 cm^{-1}): 3915(w), 3788(w), 3639(w), 3553(w), 2921 (br), 2358(w), 1632(m), 1481(w), 1449(m), 1383(s), 1295(w), 1108(w), 977(w), 806(w), 757(w), 712(m), 572(w), 510(w). EA (activated sample): Calcd for $\text{Fe}_3\text{O}(\text{H}_2\text{O})_2(\text{OH})(\text{NO}_3)_{0.22}[\text{C}_6\text{H}_3(\text{CO}_2)_3]_2 \cdot 9\text{H}_2\text{O}$: C, 26.16; H, 1.51; N, 0.37%. Found: C, 26.22; H, 1.39; N, 0.41%. Based on EA measurements, the weight percentages of MWCNTs in MWCNT/MIL-100(Fe) composites were evaluated as: 0.82% (**MC1**), 4.7% (**MC2**), and 8.08% (**MC3**).

Water adsorption measurements

Water adsorption isotherms and cycling ad-/desorption measurements were recorded using a Dynamic Vapor Sorption Analyzer (DVS Vacuum, Surface Measurement Systems Ltd, London, UK). The samples were degassed under vacuum at 120 °C for 15 h prior to commencing the appropriate experiments. For the cycling tests, samples were subjected to 21 successive ad-/desorption cycles between 40 °C and 140 °C at 5 h per cycle and a constant water vapour pressure of 5.6 kPa. The heating profile used for the test is as follows: heating from 40 °C to 140 °C at 5 °C min^{-1} , followed by an isothermal step for 90 min allowing complete desorption, and finally cooling back to 40 °C at 5 °C min^{-1} to begin water adsorption.

Results and discussion

Synthesis and structural characterization of carboxylic acid-functionalized MWCNTs

In order to synthesize the composite materials, acid-functionalized MWCNTs were first successfully prepared according to a previously reported procedure.²⁸ The purpose of functionalization was to attach carboxylic acid (COOH^-) groups on the surface of MWCNTs that can then serve as nucleation sites for *in situ* growth of MIL-100(Fe) on MWCNTs. Accordingly, the formation of carboxylic acid functionalities on the external walls of the MWCNTs was proven by FT-IR (see ESI, Fig. S2†). In the FT-IR spectrum, the $\nu_{\text{O-H}}$ stretch from the carboxylic groups was clearly observed at 3444 cm^{-1} and 2357 cm^{-1} . The latter absorption band is attributed to the $\nu_{\text{O-H}}$ stretch that arises from strongly hydrogen-bonded $-\text{COOH}$ functionalities.²⁸ Absorption bands that appeared at 2855 and 2929 cm^{-1} corresponded to H-C stretch modes of H-C=O in the carboxylate functionality. Additionally, the $\nu_{\text{C=O}}$ stretch from the carboxylate was observed at 1500 cm^{-1} . Finally, the band at 1775 cm^{-1} can be associated with the stretching of the carbon nanotube backbone in the spectra of both pristine and functionalized MWCNTs.¹⁵ Structural stability of the MWCNTs during the functionalization process was then proven *via* PXRD analysis. Specifically, diffraction peaks observed at 25.9° and 43.7°, corresponding to the (002) and (100) reflection planes, respectively, were present in both the pristine and acid-functionalized MWCNT diffraction patterns (ESI, Fig. S1†). The morphology of MWCNTs before and after the acid-treatment does not present a substantial difference except that the mutual repulsion between the negatively charged functional groups on the sidewalls facilitates the dispersion of nanotubes in aqueous medium by overcoming the van der Waals attraction between the neighbouring tubes²⁸ (ESI, Fig. S6†).

Synthesis and structural characterization of MIL-100(Fe) and MWCNT/MIL-100(Fe) composites (MC1, -2, and -3)

In this work, the synthesis of MIL-100(Fe) is based on an industrially scalable approach which is capable of a substantially high space-time-yield of $>1700 \text{ kg m}^{-3} \text{ day}^{-1}$ in the context of commercial applications of this material.³⁴

Previously, HF has been used as a mineralizing agent for the synthesis of MIL-100(Fe) with the aim of achieving a product with higher crystallinity and thus a higher expected surface area.^{29,30} The use of HF has been excluded in the method of synthesis proposed in this work considering the toxicity, corrosiveness and precautionary measures associated with the use of this chemical on a commercial scale. However, the fluorine-free MIL-100(Fe) synthesized using this approach has been reported to show comparable physicochemical properties to the material synthesized in the presence of HF.³⁴ The use of Fe(NO₃)₃·9H₂O as an iron precursor has been preferred to metallic iron in this work due to two major reasons: (a) MIL-100(Fe) synthesized using iron powder has been shown to exhibit lower yield and poor porosity,³⁴ and (b) Fe(NO₃)₃·9H₂O dissociates into Fe³⁺ ions in an aqueous medium which can interact with the COOH⁻ groups on the surface of acid-treated MWCNTs resulting in the formation of the -C-O- interface between the nanotubes and MIL-100(Fe) crystals (Scheme 1), which is not achievable through the use of metallic iron.

The method of synthesis of MWCNT/MIL-100(Fe) composites proposed in this work is based on the electrostatic interaction of oppositely charged ions in a common solvent with the aim of developing a reasonably strong interface between the nanotubes and the surrounding MOF matrix. Since this method of synthesis as well as the subsequent activation procedure are the same as those adopted for MIL-100(Fe), except for the *in situ* incorporation of acid-treated MWCNTs into the precursor solution (ESI, Fig. S3†), it can also be considered a commercially applicable method of synthesis. According to the best knowledge of the authors, such a method for the scalable synthesis of MWCNT/MIL-100(Fe) composites is being reported the first time in this work. As highlighted in Scheme 1, the purpose of acid-functionalization of MWCNTs prior to the composite synthesis is to attach COOH⁻ groups on the sidewalls, which serves the dual purpose of facilitating nanotube dispersion in an aqueous medium and acting as nucleation sites for the *in situ* growth of MIL-100(Fe) crystals on MWCNTs. This also explains why Fe(NO₃)₃·9H₂O has been preferred to metallic iron as the iron precursor, since metallic iron is incapable of dissociating into Fe³⁺ ions in an aqueous medium, which can later electrostatically bond with the COOH⁻ groups on the sidewalls of MWCNTs (ESI, Fig. S3†). As the organic linker is introduced and the reaction mixture is subjected to hydrothermal synthesis, the continuous nucleation, growth and coalescence of MIL-100(Fe) crystals at the functional sites on MWCNTs eventually result in the formation of a composite material in which the MWCNTs are implanted inside the MIL-100(Fe) framework and are chemically interfaced with the surrounding MOF matrix *via* -C-O- bonds at the same locations where COOH⁻ groups were originally present on the sidewalls (ESI, Fig. S3†). In order to gain a more generalized overview of the effect of MWCNT addition on the water adsorption properties and cyclic stability of MIL-100(Fe) for intended use as an adsorbent in a chiller application, three different MWCNT/MIL-100(Fe) composites with a low (2.16%), a medium (5.90%), and a high (10.72%) weight fraction of

MWCNTs have been synthesized using the proposed method of synthesis.

Fig. 1 shows a comparison of the PXRD patterns of MIL-100(Fe) and MWCNT/MIL-100(Fe) composites with the three different MWCNT loadings. It is noted that the PXRD pattern of MIL-100(Fe) is in good agreement with the simulated pattern from the single crystal structure (Fig. 1). However, it can be observed that both the sharpness and the intensity of the diffraction peaks slightly improve upon the gradual introduction of MWCNTs inside the MIL-100(Fe) matrix. Since the COOH⁻ groups act as nucleating sites for the crystallization and growth of MIL-100(Fe) crystals, a relatively much lower amount of free energy is required for crystal nucleation in MWCNT/MIL-100(Fe) composites as compared to MIL-100(Fe). However, since the total free energy available for nucleation, crystallization and crystal growth is roughly the same with or without the introduction of MWCNTs, a significantly greater proportion of free energy can be utilized for crystallization and growth of the crystals in the composites than that in the case of MIL-100(Fe). This eventually results in a more well-defined crystal morphology in the composites as compared to MIL-100(Fe), and hence leads to sharper and more intense diffraction peaks in the PXRD patterns of MWCNT/MIL-100(Fe) composites. It can be further noticed that the *in situ* growth of MIL-100(Fe) on functionalized MWCNTs does not result in any noticeable peak shifts or the appearance of any new peaks in the PXRD patterns of composite materials, thus preserving the structural integrity of the characteristic MIL-100(Fe) framework. Hence, it can be concluded that the proposed *in situ* synthesis method for the preparation of MWCNT/MIL-100(Fe) composites preserves the crystallinity of the framework.

The FT-IR spectra of MIL-100(Fe) as well as MWCNT/MIL-100(Fe) composites with various MWCNT loadings are

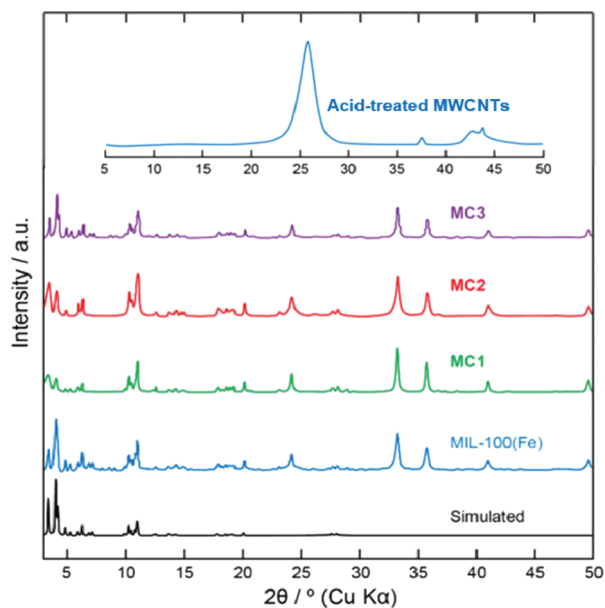


Fig. 1 PXRD patterns for MIL-100(Fe) and MWCNT/MIL-100(Fe) composites.

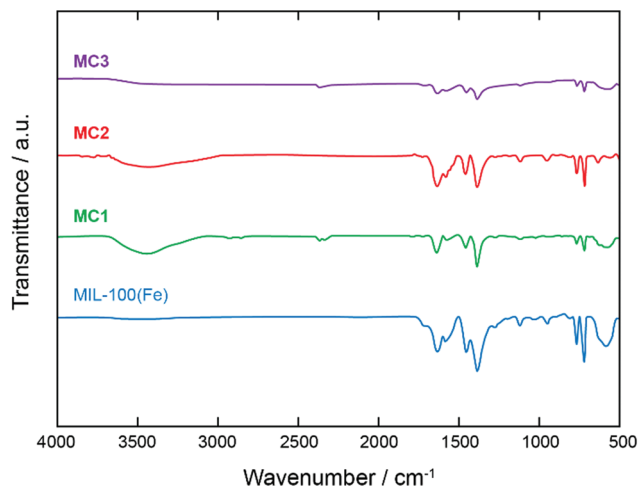


Fig. 2 FTIR spectra of MIL-100(Fe) and MWCNT/MIL-100(Fe) composites.

shown in Fig. 2. The vibrational bands evidenced around 1443, 1383, 757, and 708 cm^{-1} are characteristic of the MIL-100(Fe) framework,³² while a weak signal observed between 1710 and 1720 cm^{-1} corresponds to the traces of residual trimesic acid residing within the pores of the structure.³⁴ Finally, the broad peak observed between 2966 and 3731 cm^{-1} visible in the spectra of carbon nanotube-implanted materials is assigned to the O–H stretch coming from the unreacted carboxylic groups (O=C–OH and C–OH) present on the acid-treated MWCNTs (ESI, Fig. S2†).³¹ It can be further observed that the characteristic peak intensities continually decrease with increasing content of MWCNTs in the MIL-100(Fe) matrix. Since the MIL-100(Fe) crystals are covalently bonded to the functional sites on the surface of MWCNTs (Scheme 1d), the C–O–Fe linkages which connect the C atoms on the sidewalls of MWCNTs to the Fe metal ion centers within the framework pose a certain degree of restriction on the characteristic stretching vibrations of the bonds within the MIL-100(Fe) framework. Since the intensity of an absorption band in the FTIR spectrum depends on the change in the bond dipole moment, which is directly proportional to the change in the bond length occurring during bond stretching, the more constrained stretching vibrations of the bonds in MWCNT/MIL-100(Fe) composites as compared to MIL-100(Fe) thus lead to reduced amounts of changes in the dipole moments of the bonds within the framework, and correspondingly lower peak intensities in the FTIR spectra than those observed in the spectrum of pristine MIL-100(Fe). More interestingly, a faint shoulder is observed between 510 and 515 cm^{-1} in the spectrum of MC3, which is totally absent in the spectrum of MIL-100(Fe) (ESI, Fig. S4†). This peak corresponds to the C–O–Fe bending vibration, which is a consequence of the chemical coordination formed between the negatively charged carboxylic groups on the acid-treated MWCNTs, and the positively charged Fe^{3+} ions during the *in situ* synthesis of the composite.^{26,33}

In order to further probe the chemistry of the interface between the MWCNTs and the surrounding MOF matrix, XPS measurements were conducted on the acid-treated MWCNTs, MIL-100(Fe), and MC3. The full survey of the surface composition for MIL-100(Fe) and MC3 shows photoelectron lines at a binding energy of about 283.15, 530.31 and 710.53 eV, which are attributed to C 1s, O 1s and Fe 2p, respectively,³⁵ while the full survey for acid-treated MWCNTs shows lines at about 530.64 and 282.63 eV, which correspond to O 1s and C 1s, respectively (ESI, Fig. S5†).³⁶ The O 1s peak of acid-treated MWCNTs can be deconvoluted into 3 peaks centered at 531.63, 533.55 and 533.17 eV, which represent the phenol, carboxyl and carbonyl groups, respectively, while the C 1s peak can be deconvoluted into 4 peaks centered at 286.17, 284.92, 286.66 and 284.61 eV, which are attributable to C=O, C–C, C–O and C=C bonds, respectively (ESI, Table S2†).³⁶ For MIL-100(Fe), the C 1s peak can be deconvoluted into 3 peaks centered at 282.95, 286.88 and 284.61 eV, representing phenyl, carboxyl, and surface C atoms, respectively.³⁵ In the case of MC3, the peaks corresponding to carboxyl groups and surface C atoms are positioned at more or less the same binding energies as in MIL-100(Fe); however, the peak representing the phenyl group in MIL-100(Fe) is further deconvoluted into two peaks centered at 283.20 and 282.57 eV in MC3 (ESI, Fig. S5†), which is attributable to the attachment of functional moieties at two distinct positions on the benzene ring caused by the shift in the mechanism of formation of MIL-100(Fe) crystals occurring due to the introduction of MWCNTs (Scheme 1d).^{35,37} The O 1s peak of MIL-100(Fe) can be deconvoluted into 3 peaks centered at 530.37, 532.29 and 530.20 eV, which correspond to C=O, C–O–Fe and O–Fe bonds, respectively, and are positioned at 530.69, 528.61 and 530.36 eV, respectively, in the case of MC3 (ESI, Fig. S5†). Hence, the peak attributable to C–O–Fe bonds in the MIL-100(Fe) framework shifts to a lower binding energy in MC3 as the O atoms require additional valence electrons in order to form covalent bonds with Fe atoms, resulting in the interfacial C–O–Fe bonds between the MWCNTs and the MIL-100(Fe) crystals (Scheme 1d). The Fe 2p peak for MIL-100(Fe) can be deconvoluted into 4 peaks centered at 709.83, 712.12, 724.01 and 715.72 eV, corresponding to the peaks of Fe 2p_{3/2}, Fe 2p_{1/2}, and the two satellite peaks of Fe 2p_{1/2} and Fe 2p_{3/2}, respectively (ESI, Fig. S5†).³⁵ For MC3, the same peaks are observed at 709.65, 711.86, 723.44 and 716.35 eV, respectively (ESI, Table S2†). Hence, the satellite peak of Fe 2p_{3/2} for MIL-100(Fe) shifts to a higher binding energy in the case of MC3, since removal of additional valence electrons from Fe atoms to form bonds with COOH^- groups on the surface of acid-treated MWCNTs is expected to increase the binding energy of the core electrons, and correspondingly shift the satellite peak of Fe 2p_{3/2} to a higher binding energy.³⁷

Electron microscopy analysis of MC1, -2, and -3

The morphologies of MIL-100(Fe) and MWCNT/MIL-100(Fe) composites observed by SEM are shown in Fig. 3. The octahedral-shaped crystals' characteristics of MIL-100(Fe) are

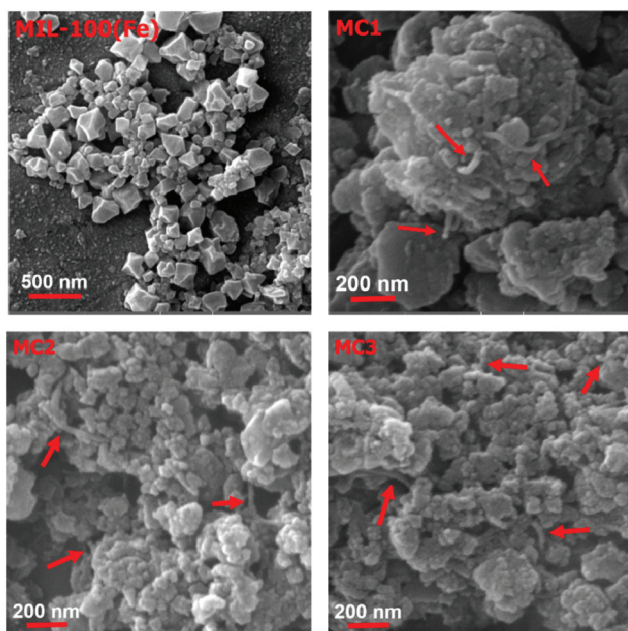


Fig. 3 SEM micrographs of MIL-100(Fe) and MWCNT/MIL-100(Fe) composites (red arrows indicate the presence of MWCNTs).

evident in the SEM image of MIL-100(Fe). However, a significant degree of variation can be seen in the size of the crystals, which is observed to lie between 50 nm and 500 nm in terms of diameter. The incorporation of MWCNTs preserves the shape of the MIL-100(Fe) crystals as shown in the SEM images of MC1–MC3. However, a change in the crystallite size can be observed due to the incorporation of MWCNTs with gradually increasing loading inside MIL-100(Fe). In general, it was observed that increasing the weight fraction of MWCNTs tends to reduce the average crystallite size of MIL-100(Fe) in the MWCNT/MIL-100(Fe) composites. The MWCNTs can also be seen implanted in the surrounding MIL-100(Fe) matrix, which can be regarded as a consequence of the synthesis protocol adopted for the MWCNT/MIL-100(Fe) composites (ESI, Fig. S3†). However, since the nanotubes are completely covered by the MIL-100(Fe) crystallites (Scheme 1d), the typical tubular morphology characteristic of the MWCNT structure cannot be evidenced clearly in the SEM micrographs of the MWCNT/MIL-100(Fe) composites shown in Fig. 3. Due to this reason, the presence of MWCNTs has been highlighted using the red arrows in the micrographs of the composites. The atomic percentages of Fe, C, and O in MIL-100(Fe) and MC1–MC3 have been measured using EDS analysis. As expected, the Fe content measured using EDS can be seen to decrease continually with increasing content of MWCNTs in MIL-100(Fe); however, consistency in terms of C contents cannot be seen since EDS is well-known for its inaccuracy in this context (ESI, Fig. S7†). It can be further observed that the difference between the MWCNT contents measured using EA and EDS reduces as the weight percentage of MWCNTs is increased in MWCNT/MIL-100(Fe) composites (ESI, Table S3†).

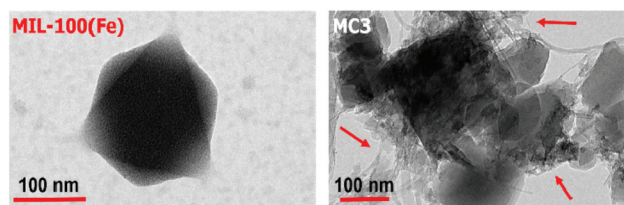


Fig. 4 TEM micrographs of MIL-100(Fe) and MWCNT/MIL-100(Fe) composites (red arrows indicate points of MWCNT agglomeration).

In order to gain a better insight into the morphology of the MWCNT/MIL-100(Fe) composite, TEM images of MIL-100(Fe) as well as MC3 were taken as shown in Fig. 4. Since the electron beam used in TEM transmits through the thickness of the sample, the cross-section of one of the octahedral crystals of MIL-100(Fe) shown in Fig. 3 can be clearly seen in the TEM image of MIL-100(Fe) shown in Fig. 4. The TEM image of MC3, shown in Fig. 4, re-confirms the implantation of MWCNTs in the MOF matrix, which can be clearly seen as tubular structures spread across the cross-section of the octahedral crystals of MIL-100(Fe). However, due to the relatively higher proportion of MWCNTs in MC3, agglomeration of MWCNTs in certain regions was observed, indicated by the red arrows in the TEM micrograph shown in Fig. 4.

Architectural robustness of MIL-100(Fe) and MC-1, -2, and -3

The thermogravimetric analysis (TGA) results of acid-treated MWCNTs, MIL-100(Fe) and MWCNT/MIL-100(Fe) composites are shown in Fig. 5. For MIL-100(Fe), the TGA curve exhibits three major weight losses spread between 30 and 700 °C.³⁴ However, for the composite materials, an additional weight loss is observed owing to the presence of MWCNTs in the framework. An initial weight loss between 30 and 60 °C corresponds to the removal of water molecules trapped inside the pores within the MIL-100(Fe) framework. The second weight loss spread between 60 °C and 297 °C represents the evaporation of water molecules coordinated to the iron trimer clusters. The abrupt weight loss of 32.23% observed between 297 °C and 353 °C in the TGA profile of MIL-100(Fe) is

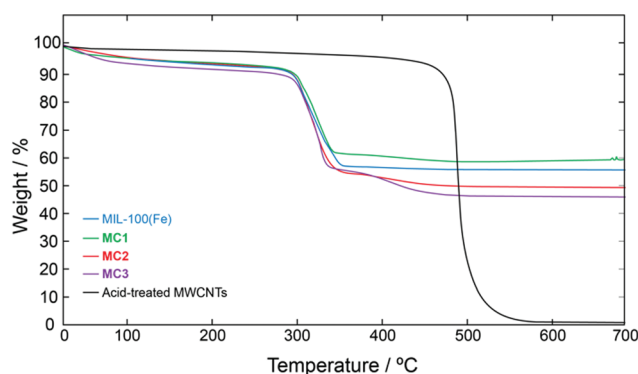


Fig. 5 TGA of acid-treated MWCNTs, MIL-100(Fe), and MWCNT/MIL-100(Fe) composites in air.

assigned primarily to linker decomposition within the framework.³⁴ However, the linker decomposition start and end temperatures were observed to vary with changing content of MWCNTs in MWCNT/MIL-100(Fe) composites. In general, it was noticed that the temperature at which the linker decomposition ends (or the MWCNT oxidation begins) shifts to lower values with increasing content of MWCNTs in MIL-100(Fe) (ESI, Table S1†). Above the linker decomposition end temperature up to the final analysis temperature of 700 °C, the weight loss occurring in all the composite samples is assigned primarily to the oxidation of MWCNTs with a negligibly small contribution corresponding to the decomposition of the remaining linker. The orange-coloured residue recovered after the TGA of all the samples was identified to be iron oxide (Fe₂O₃) using PXRD (ESI, Fig. S8†). Since the residual weight of functionalized MWCNTs at 700 °C was measured to be 0.75 wt% (ESI, Fig. S9†), the weight percentage of MWCNTs in each composite sample can be calculated using eqn (S1). As shown in Table 1, the percentages of MWCNTs in the composites based on TGA data are evaluated to be 2.16, 5.90, and 10.72 wt% for **MC1**, **MC2** and **MC3** respectively. For further confirming the content of MWCNTs in MWCNT/MIL-100(Fe) composites, elemental analysis (EA) was carried out on all the activated samples and the results are also shown in Table 1. It can be noticed that the EA results follow a similar trend to that observed for the TGA results. However, the weight percentages of MWCNTs in MWCNT/MIL-100(Fe) composites in this work have been evaluated using TGA results since EA-based compositions rely only on the presence of C, H, N, and S inside a material, while the synthesized MOF composites also incorporate substantial amounts of O and Fe.

The nitrogen adsorption–desorption isotherms of MIL-100(Fe) as well as MWCNT/MIL-100(Fe) composites at 77 K are shown in Fig. 6. It is noticeable that the isotherms reveal a typical type-IV behaviour indicative of a mesoporous framework. It can be clearly seen that increasing the content of MWCNTs in the MIL-100(Fe) matrix does not introduce any further hysteresis. In other words, the incorporation of MWCNTs preserves the intrinsic porosity of the MIL-100(Fe) framework. The specific surface area for MIL-100(Fe) was found to be equal to 1360 m² g⁻¹, which is in good agreement with the already published data for MIL-100(Fe) synthesized using the same procedure.³⁴ The total pore volume was taken by a single-point method at $P/P_0 = 0.9$ to exclude external surface area effects caused by the presence of extra small particles (<80 nm) (Fig. 3).³⁸ Table 2 lists the BET surface areas and total pore volumes of all the samples calculated from their

Table 1 Comparison of MWCNT contents (wt%) in MWCNT/MIL-100(Fe) composites calculated using TGA and EA data

Sample ID	TGA	EA
MC1	2.16	0.82
MC2	5.90	4.70
MC3	10.72	8.08

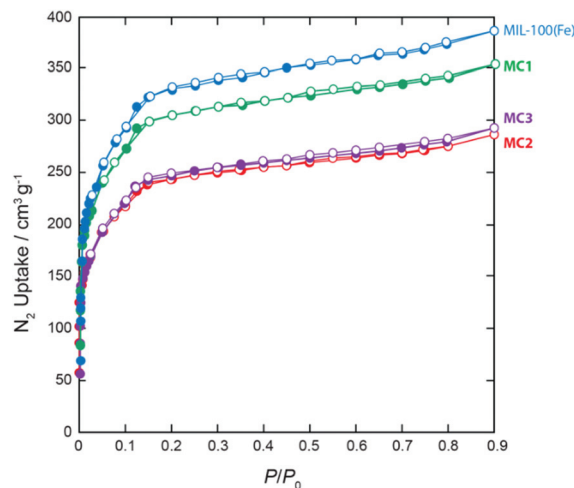


Fig. 6 N₂ adsorption–desorption isotherms at 77 K for MIL-100(Fe) and MWCNT/MIL-100(Fe) composites.

Table 2 BET surface areas ($P/P_0 = 0.06–0.2$) and total pore volume ($P/P_0 = 0.9$) of MIL-100(Fe) and MWCNT/MIL-100(Fe) composites calculated from the respective nitrogen adsorption isotherms at 77 K

Sample ID	S_{BET} (m ² g ⁻¹)	V_{T} (cm ³ g ⁻¹)
MIL-100(Fe)	1360	0.832
MC1	1139	0.697
MC2	999	0.611
MC3	1022	0.625

respective nitrogen adsorption–desorption isotherms at 77 K. As expected, it is noticed that all the MWCNT/MIL-100(Fe) composites exhibit lower surface areas than MIL-100(Fe). The surface area for the composites first decreases gradually from **MC1** to **MC2** and then again increases for **MC3**. Since the *in situ* synthesis process involves the nucleation and growth of MIL-100(Fe) crystals at the acid-treated sites on the surface of functionalized MWCNTs, a high probability of interference of the nanotube structure with the intrinsic porosity of the MIL-100(Fe) framework exists, which is a possible cause of the decrease in the surface area observed for **MC1** to **MC2**.^{26,27} However, upon exceeding a critical weight fraction of MWCNTs, the increase in the nucleation rate of MOF crystals over the sidewalls of MWCNTs is expected to surpass the interference effect of MWCNTs on the intrinsic porosity, causing a subsequent increase in surface area as observed in the case of **MC3**.

Specific heat capacities of MIL-100(Fe) and MWCNT/MIL-100(Fe) composites

The specific heat capacities of acid-treated MWCNTs, MIL-100(Fe) and MWCNT/MIL-100(Fe) composites as a function of temperature are shown in Fig. 7. The specific heat capacity, C_p , values have been calculated indirectly from DSC data using eqn (S2).³⁹ It can be seen that C_p increases gradually with temperature for all materials except the acid-treated MWCNTs

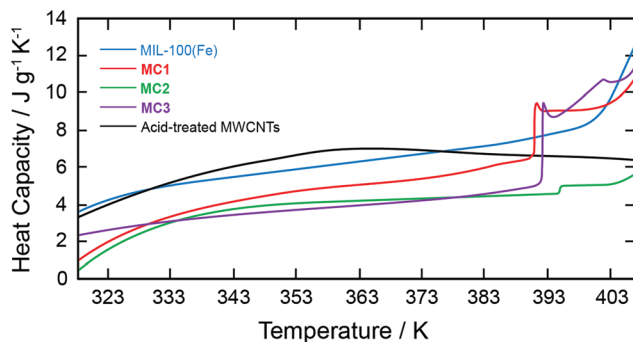


Fig. 7 Specific heat capacities as a function of temperature for acid-treated MWCNTs, MIL-100(Fe) and MWCNT/MIL-100(Fe) composites.

in which case it starts to decrease after a certain temperature between 90 and 100 °C is reached. For MWCNT/MIL-100(Fe) composites, a threshold temperature is required for phonon-nanotube interaction to initiate since the MWCNTs are implanted inside the MOF crystals (Fig. 3 and 4). As soon as this temperature is reached, an abrupt rise in C_p can be seen in Fig. 7 for the three types of composite materials. This temperature can be observed to lie between 120 and 130 °C for **MC1**, and between 110 and 120 °C for both **MC2** and **MC3**. As soon as the entire length of a given MWCNT is fully traversed, the phonons again reach the neighbouring MIL-100(Fe) crystal, resulting in a sudden drop in the value of C_p , followed by the formal gradual rise with temperature as observed in the case of **MC2** and **MC3**.

Water adsorption/desorption kinetics and cyclic stability of MIL-100(Fe) and MWCNT/MIL-100(Fe) composites

Amongst the water-stable MOFs reported so far, MIL-101(Cr) has been shown to exhibit the highest water vapour uptake as well as hydrothermal stability followed by MIL-100(Fe).^{7,11,40–42,47} However, the inherent environmental toxicity associated with Cr metal limits the use of MIL-101(Cr) as a potential adsorbent for commercial chiller applications.⁴³ Hence, MIL-100(Fe) currently appears to be the most appropriate candidate amongst water-stable MOFs for potential use as an adsorbent in a chiller application. However, as mentioned earlier, the intrinsic low ad-/desorption rates of water vapour associated with this material due to inferior thermal characteristics still need to be addressed as these limitations can adversely affect both the coefficient of performance and the specific cooling power.^{10–20} In this context, the incorporation of MWCNTs in a MIL-100(Fe) framework is being introduced for the first time in this work with the aim of improving the thermal properties of this material without adversely affecting its intrinsic water adsorption behaviour or hydrothermal cyclic stability. In other words, a trade-off exists between the amount of MWCNTs which can be introduced in MIL-100(Fe) without deteriorating the intrinsic porosity of the framework and the degree of enhancement which can be achieved in the thermal properties of the resulting composite.

The water adsorption/desorption isotherms at 298 K for MIL-100(Fe) and MWCNT/MIL-100(Fe) composites are shown in Fig. 8. A maximum water vapour uptake of 42.45 wt% is observed for MIL-100(Fe), which drops to 24.72 wt% after the framework is subjected to 21 consecutive water adsorption/desorption cycles between 313 and 413 K as shown in Fig. 8(a). It can be observed that there is a steep rise in water uptake for $0.3 < P/P_0 < 0.4$, which is in agreement with the already published literature.^{6,44} At $P/P_0 < 0.25$, mono- and multi-layer adsorption of water molecules mainly takes place at the hydrophilic metal ion clusters within the framework. The steep rise observed between $0.3 < P/P_0 < 0.4$ is attributed to capillary condensation, which first involves the filling of 25 Å mesopores, followed by the filling of 29 Å mesopores.⁴⁴ For MWCNT/MIL-100(Fe) composites, the steep rise observed between $0.3 < P/P_0 < 0.4$ as well as the shape of the isotherms are not affected by the presence of MWCNTs, which implies that the water adsorption kinetics remain more or less the same as for MIL-100(Fe). The maximum uptakes are observed to be 38.77 wt% (**MC1**), 42.96 wt% (**MC2**), and 40.86 wt% (**MC3**). Hence, **MC2** results in a 1.2% higher maximum water vapour uptake than MIL-100(Fe) at 298 K despite the intrinsic hydrophobic nature of MWCNTs. This is attributable to a relatively higher nucleation rate of MIL-100(Fe) on the surface of MWCNTs resulting in a relatively larger number of crystals, and consequently a greater number of sites available for water adsorption (Fig. 3).⁴⁵ However, on exceeding a critical weight fraction of MWCNTs, the increase in hydrophobicity of the framework supersedes the effect of the higher nucleation rate of MIL-100(Fe) crystals, thus again causing a reduction in maximum water vapour uptake.⁴⁵ The other factor that might lead to lower uptake at higher MWCNT contents as discussed above is agglomeration.⁴⁶ Since the mean inter-tube distance varies inversely with the percentage of MWCNTs in the composites, a sufficiently higher loading might cause the inter-tube distance to reduce to an extent at which the van der Waals attraction between the neighbouring tubes might overcome the mutual repulsion caused by the COO[−] groups on the side-walls, thus eventually leading towards agglomeration.⁴⁶ As a result, the density of tube-free regions will greatly exceed the density of agglomerated regions in the composites, thus lowering the net nucleation rate of MIL-100(Fe) crystals on MWCNTs and a subsequent reduction in water vapour uptake. A comparison of adsorption isotherms measured at 298 and 313 K reveals that both MIL-100(Fe) and **MC1** show noticeably different adsorption kinetics and lower water vapour uptake at 313 K, while both **MC2** and **MC3** exhibit very similar adsorption kinetics as well as water vapour uptakes as the temperature is increased from 298 to 313 K (ESI, Fig. S10†).

Another intrinsic property which can be affected by the hydrophobicity of MWCNTs in MWCNT/MIL-100(Fe) composites is the isosteric heat or enthalpy of adsorption, $Q_{st,ads}$. Since heat of adsorption is a measure of the affinity of an adsorbent towards adsorbate molecules, the concept of $Q_{st,ads}$ becomes even more significant in MWCNT/MIL-100(Fe) composites due to the intrinsic hydrophobic nature of MWCNTs.

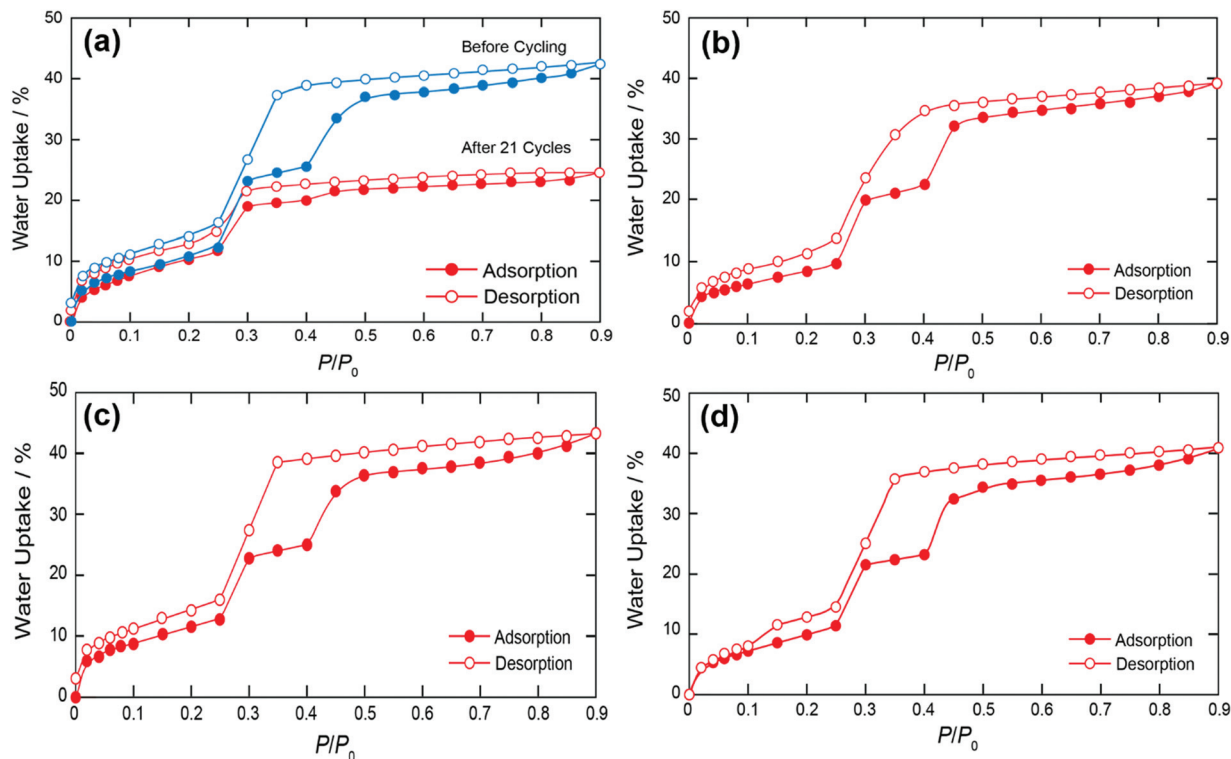


Fig. 8 Water adsorption–desorption isotherms for (a) MIL-100(Fe), (b) MC1, (c) MC2 and (d) MC3 at 298 K.

Hence, a noticeably different variation of $Q_{st,ads}$ with instantaneous water uptake can be expected for MWCNT/MIL-100(Fe) composites as compared to MIL-100(Fe) (ESI, Fig. S11†). In the context of a chiller application, the average value of $Q_{st,ads}$ can further prove beneficial in estimating the power capability (P.C.) of a given adsorbent if the average adsorption–desorption cycle time required to reach a pre-determined value of adsorbate uptake during the chiller operation is already known.⁴⁸ The important parameters related to water adsorption kinetics, along with isosteric heats of adsorption and power capability for MIL-100(Fe) and MWCNT/MIL-100(Fe) composites, are listed in Table 3, where the values of $Q_{st,ads}$ and P.C. have been calculated using eqn (S3) and (S4) respectively. It can be seen that the water uptakes at 298 and 313 K

as well as the values of $Q_{st,ads}$ follow the same trend as the content of MWCNTs is gradually increased, *i.e.*, an initial drop is observed from MIL-100(Fe) to MC1, followed by an increase from MC1 to MC2, and a final drop from MC2 to MC3. The highest value of $Q_{st,ads}$ is exhibited by MC2, which also shows the highest water vapour uptake at both 298 and 313 K. However, the highest value of P.C. has been evaluated for MC1 despite showing the lowest water vapour uptake amongst the four types of materials (ESI, Table S4†). This shows that cyclic stability plays an equally important role for an adsorbent material to achieve an uninterrupted and a reasonably long-term performance in a commercial-scale chiller application.

Apart from being sufficiently hydrophilic for achieving a high water uptake at relatively lower relative pressures, an adsorbent material needs to remain structurally stable on exposure to repeated ad-/desorption cycles for successful use in a chiller application. The evaluation of hydrothermal cyclic stability is thus a necessary and an important prerequisite to assess the feasibility of an adsorbent material for long-term use in a chiller application.^{11,49–51} The cyclic water adsorption/desorption test results based on 21 consecutive cycles for MIL-100(Fe) and MWCNT/MIL-100(Fe) composites are shown in Fig. 9. It can be seen that there is a continual decrease in water vapour uptake with increasing the number of cycles for each type of material. For MIL-100(Fe), it is observed that there is a difference of 48.20% between the maximum water vapour uptake measured for the first and the last cycles; for MC1, this difference was evaluated to be equal to 37.73%; for MC2 it was

Table 3 Important water adsorption parameters, isosteric heats of adsorption and power capability values for MIL-100(Fe) and MWCNT/MIL-100(Fe) composites

Sample ID	α^a	Water uptake at 298 K (%)	Water uptake at 313 K (%)	$Q_{st,ads}$ (kJ mol ⁻¹)	P.C. (W kg ⁻¹)
MIL-100(Fe)	0.285	42.45	36.16	51.19	1.03
MC1	0.300	38.77	34.59	49.32	1.78
MC2	0.294	42.96	42.26	55.32	1.28
MC3	0.294	40.86	39.66	40.88	1.33

^a Relative pressure P/P_0 at which the adsorbed amount at 298 K is a half of the adsorbed amount at $P/P_0 = 0.9$.

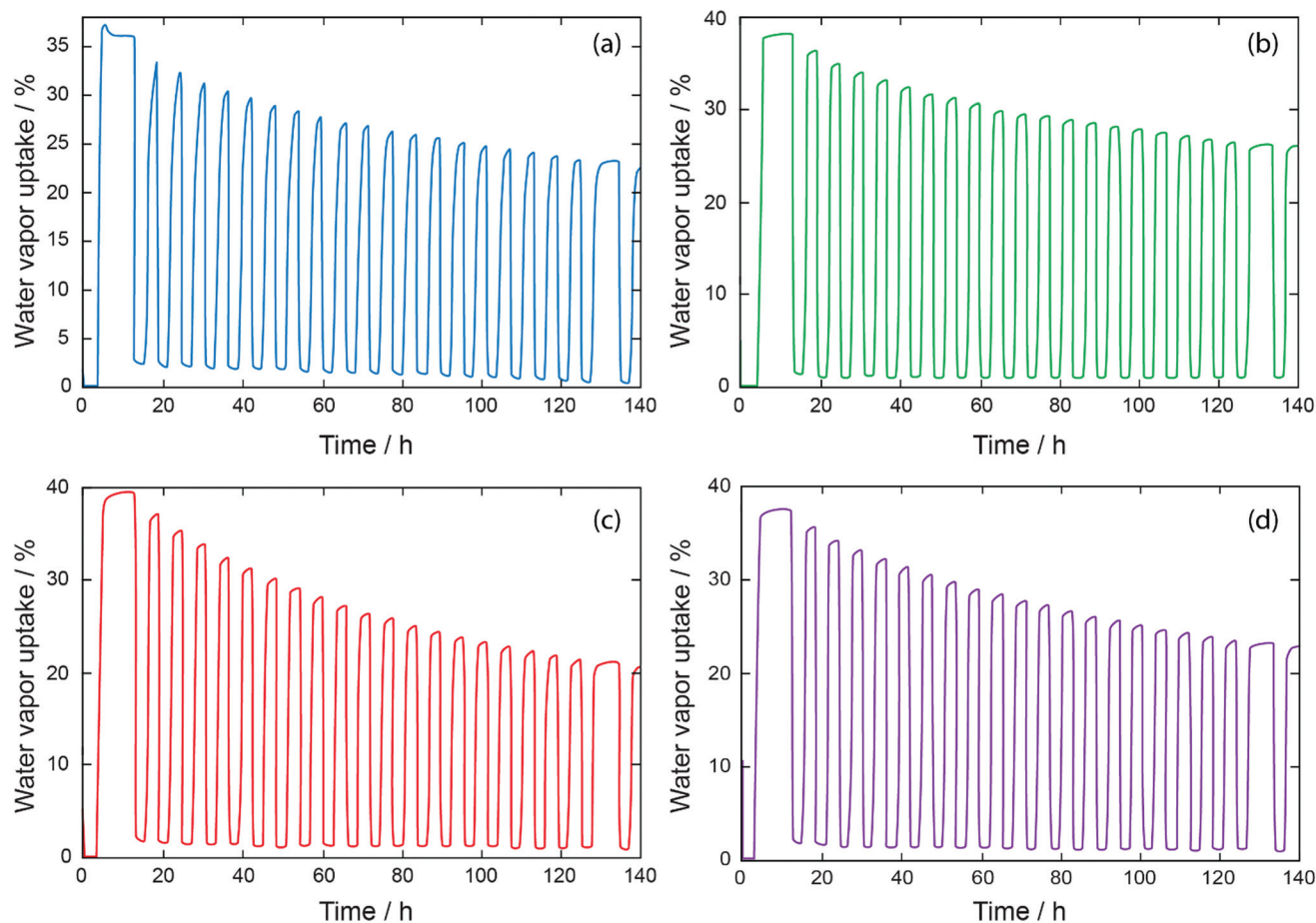


Fig. 9 Cyclic adsorption–desorption profiles for 21 cycles: (a) MIL-100(Fe), (b) MC1, (c) MC2 and (d) MC3.

calculated to be equal to 62.54%, while for MC3 it was evaluated to be equal to 48.43%. Hence, a comparison of Fig. 8 and 9 indicates that the composite exhibiting the highest maximum water vapour uptake at 298 K also results in the largest difference between the maximum uptake measured for the first and the last cycles during cyclic adsorption–desorption (MC2), while the one exhibiting the lowest maximum water vapour uptake results in the smallest difference between the maximum uptake measured for the first and the last cycles (MC1). A comparison of Fig. 8 with Table 3 indicates that a direct correlation exists between the percentage of residual water molecules retained inside the pores at the end of adsorption–desorption isotherms measured at 298 K and the value of $Q_{st,ads}$ measured for each material (ESI, Table S5[†]). In the context of cyclic adsorption/desorption, if the amount of residual water molecules left inside the pores at the end of the first adsorption–desorption cycle increases, the number of pores which are already filled before the start of the second cycle also increases, and hence the percentage of the amount of water adsorbed during the second cycle is correspondingly smaller than the first cycle. As this process continues for a subsequent number of cycles, the percentage decrease in water uptake keeps on accumulating until a substantially large

percentage difference in water uptake can be observed between the first and the last cycle as noticed in the case of MC2. MC3 should, however, be regarded as an exemption in this context owing to the apparent agglomeration of MWCNTs observed inside this material (Fig. 4).

As shown in Table 3, the lowest value of P.C. amongst the three types of composites is shown by MC2, while the highest value is exhibited by MC1. The authors, therefore, recommend a MWCNT content between 2 and 6 wt% in MWCNT/MIL-100 (Fe) composites for successful use as an adsorbent material in an adsorption chiller application; however, this still requires further investigation in terms of scalability towards a commercial system. The SEM micrographs taken on the cycled samples indicate that both MIL-100(Fe) and MWCNT/MIL-100 (Fe) composites retain their characteristic lattice morphologies after exposure to repeated adsorption–desorption cycles. However, the MWCNTs shown in the micrographs of the cycled materials become more evident than the uncycled counterparts owing to the partial disintegration of some of the surrounding MIL-100(Fe) crystallites upon repeated exposure to the cycling procedure (ESI, Fig. S12[†]). A comparison of the PXRD profiles of the four cycled materials with their uncycled counterparts indicates that each retains its characteristic

lattice structure even after being subjected to 21 consecutive adsorption–desorption cycles between 313 and 413 K (ESI, Fig. S13†).

Conclusions

A novel *in situ* method for the synthesis of MWCNT/MIL-100(Fe) composites based on the molecular level interaction of Fe³⁺ ions with COOH[−] groups on the surface of acid-treated MWCNTs has been presented. The proposed method results in successful implantation of MWCNTs within the MIL-100(Fe) framework as confirmed by the SEM and TEM micrographs of the as-synthesized composite samples. The incorporation of MWCNTs preserves the characteristic lattice structure of the framework as confirmed by the PXRD patterns of the activated MOF materials. The BET surface area for the composites measured using nitrogen physisorption isotherms at 77 K first decreases for 2.16 to 5.9 wt% MWCNTs in MIL-100(Fe), then again increases for 10.72 wt%. However, the characteristic type-IV shape of the isotherm for MIL-100(Fe) is maintained for all the three types of activated composite materials. From the TGA profiles measured for MWCNT/MIL-100(Fe) composites, it has been observed that the temperature at which the linker decomposition ends (or the MWCNT oxidation begins) shifts to lower values with increasing content of MWCNTs in MIL-100(Fe). The FTIR spectra taken for the carbon nanotube-incorporated materials reveal no additional signals other than those corresponding to the functional groups characteristic of the MIL-100(Fe) framework, or those attached to the sidewalls of functionalized MWCNTs, suggesting that the chemical integrity of the structure is preserved upon the incorporation of MWCNTs using the proposed method of synthesis. As part of investigating the nature of the interface formed between the host and the guest species, an XPS analysis has been conducted which confirms the existence of C–O–Fe bonding between the MWCNTs and MIL-100(Fe) crystals revealed earlier by the FTIR study.

From the water adsorption–desorption kinetics study, a maximum water vapour uptake of 42.45% has been measured for MIL-100(Fe), which drops to 24.72% after the framework is subjected to 21 consecutive water adsorption/desorption cycles. For MWCNT/MIL-100(Fe) composites, the maximum uptakes have been observed to be 38.77% (2.16 wt%), 42.96% (5.90 wt%), and 40.86% (10.72 wt%). From the cyclic water adsorption–desorption tests conducted between 313 and 413 K, a difference of 54.31% between the maximum water vapour uptake for the first and the last cycles has been measured for MIL-100(Fe) while for 2.16, 5.9, and 10.72 wt% MWCNT/MIL-100(Fe) composites, this was observed to be 37.73%, 62.54%, and 48.43% respectively. Hence, the composite exhibiting the highest water vapour uptake at 298 K also results in the largest difference between the uptakes measured for the first and the last cycles during cyclic adsorption–desorption, while the one exhibiting the lowest water vapour uptake results in the smallest difference between the uptakes

measured for the first and the last cycles. However, the composite showing the lowest uptake also results in the highest power capability, while the one showing the highest uptake also results in the lowest power capability measured for the three types of composites. Hence, for practical use as an adsorbent in an adsorption chiller application, a MWCNT content between 2 and 6 wt% in MWCNT/MIL-100(Fe) composites is recommended in order to achieve a reasonable compromise between a high water uptake, cyclic stability and power capability in the context of a commercial system. The outcome of the study suggests that the proposed MWCNT/MIL-100(Fe) composites synthesized using the proposed approach can be considered a viable alternative for conventionally used zeolite- and silica-gel-based adsorbents for use in commercial-scale adsorption chillers using water as a refrigerant.

Acknowledgements

The authors are highly grateful for the technical support granted by the Center of Research Excellence in Renewable Energy, the Center for Carbon Capture and Sequestration, the Center of Engineering Research, and the Center of Excellence in Nanotechnology, Research Institute, King Fahd University of Petroleum and Minerals, in all phases of preparation of the manuscript. We acknowledge Prof. O. M. Yaghi and Mr K. E. Cordova (UC Berkeley) for their valuable inputs regarding this work.

Notes and references

- 1 R. G. Oliveira, R. Z. Wang, J. K. Kiplagat and C. Y. Wang, *Renewable Energy*, 2009, **34**, 2757.
- 2 H. Huang, T. Oike, F. Watanabe, Y. Osaka, N. Kobayashi and M. Hasatani, *Appl. Therm. Eng.*, 2010, **30**, 1193.
- 3 L. W. Wang, Z. Tamainot-Telto, R. Thorpe, R. E. Critoph, S. J. Metcalf and R. Z. Wang, *Renewable Energy*, 2011, **36**, 2062.
- 4 X. B. Bu, Z. N. Lu and L. B. Wang, *Sci. Bull.*, 2013, **58**, 3709.
- 5 S. K. Henninger, F. Jeremias, J. Ehrenmann and C. Janiak, in International Sorption Heat Pump Conference, Italy, 2011, p. 415.
- 6 F. Jeremias, A. Khutia, S. K. Henninger and C. Janiak, *J. Mater. Chem.*, 2012, **22**, 10148.
- 7 S. K. Henninger, F. Jeremias, H. Kummer and C. Janiak, *Eur. J. Inorg. Chem.*, 2012, **2012**, 2625.
- 8 G. Akiyama, R. Matsuda and S. Kitagawa, *Chem. Lett.*, 2010, **39**, 360.
- 9 J. Ehrenmann, S. K. Henninger and C. Janiak, *Eur. J. Inorg. Chem.*, 2011, **2011**, 471.
- 10 S. K. Henninger, G. Munz, K.-F. Ratzsch and P. Schossig, *Renewable Energy*, 2011, **36**, 3043.
- 11 F. Jeremias, D. Fröhlich, C. Janiak and S. K. Henninger, *New J. Chem.*, 2014, **38**, 1846.

- 12 M. F. de Lange, B. L. van Velzen, C. P. Ottevanger, K. J. F. M. Verouden, L.-C. Lin, T. J. H. Vlugt, J. Gascon and F. Kapteijn, *Langmuir*, 2015, **31**, 12783.
- 13 S. K. Henninger, H. A. Habib and C. Janiak, *J. Am. Chem. Soc.*, 2009, **131**, 2776.
- 14 S. K. Henninger, F. Jeremias, H. Kummer, P. Schossig and H.-M. Henning, *Energy Procedia*, 2012, **30**, 279.
- 15 C. Janiak and S. K. Henninger, *Chimia*, 2013, **67**, 419.
- 16 M. F. de Lange, PhD thesis, Delft University of Technology, 2015.
- 17 A. Rezk, R. Al-Dadah, S. Mahmoud and A. Elsayed, *Int. J. Heat Mass Transfer*, 2012, **55**, 7366.
- 18 A. Rezk, R. Al-Dadah, S. Mahmoud and A. Elsayed, *Proc. Inst. Mech. Eng., Part C*, 2012, **27**, 992.
- 19 A. Rezk, R. Al-Dadah, S. Mahmoud and A. Elsayed, *Appl. Energy*, 2013, **112**, 1025.
- 20 J. Canivet, A. Fateeva, Y. Guo, B. Coasne and D. Farrusseng, *Chem. Soc. Rev.*, 2014, **43**, 5594.
- 21 F. Jeremias, S. K. Henninger and C. Janiak, *Chem. Commun.*, 2012, **48**, 9708.
- 22 D. Liu, J. J. Purewal, J. Yang, A. Sudik, S. Maurer, U. Mueller, J. Ni and D. J. Siegel, *Int. J. Hydrogen Energy*, 2012, **37**, 6109.
- 23 Y.-Z. Zhang, T. Cheng, Y. Wang, W.-Y. Lai, H. Pang and W. Huang, *Adv. Mater.*, 2016, **28**, 5242.
- 24 B. Li, M. Zheng, H. Xue and H. Pang, *Inorg. Chem. Front.*, 2016, **3**, 175.
- 25 H. Pang, B. Li, Q. Zhao, W.-Y. Lai and W. Huang, *J. Mater. Chem. A*, 2016, **4**, 4840.
- 26 Y. Yang, L. Ge, V. Rudolph and Z. Zhu, *Dalton Trans.*, 2014, **43**, 7028.
- 27 K. P. Prasanth, P. Rallapalli, M. C. Raj, H. C. Bajaj and R. V. Jasra, *Int. J. Hydrogen Energy*, 2011, **36**, 7594.
- 28 S. Goyanes, G. R. Rubiolo, A. Salazar, A. Jimeno, M. A. Corcuera and I. Mondragon, *Diamond Relat. Mater.*, 2007, **16**, 412.
- 29 K. Barthelet, J. Marrot, D. Riou and G. Férey, *Angew. Chem., Int. Ed.*, 2002, **41**, 281.
- 30 C. Serre, F. Millange, C. Thouvenot, M. Noguès, G. Marsolier, D. Louer and G. Férey, *J. Am. Chem. Soc.*, 2002, **124**, 13519.
- 31 W. M. Davis, C. L. Erickson, C. T. Johnston, J. J. Delfino and J. E. Porter, *Chemosphere*, 1999, **38**, 2913.
- 32 R. Liang, R. Chen, F. Jing, N. Qin and L. Wu, *Dalton Trans.*, 2015, **44**, 18227.
- 33 M. G. I. Galinato, C. M. Whaley and N. Lehnert, *Inorg. Chem.*, 2010, **49**, 3201.
- 34 Y.-K. Seo, J. W. Yoon, J. S. Lee, U.-H. Lee, Y. K. Hwang, C.-H. Jun, P. Horcajada, C. Serre and J.-S. Chang, *Microporous Mesoporous Mater.*, 2012, **157**, 137.
- 35 F. Zhang, J. Shi, Y. Jin, Y. Fu, Y. Zhong and W. Zhu, *Chem. Eng. J.*, 2015, **259**, 183.
- 36 T. I. T. Okpalugo, P. Papakonstantinou, H. Murphy, J. McLaughlin and N. M. D. Brown, *Carbon*, 2005, **43**, 153.
- 37 K. Y. Lee, M. Kim, J. Hahn, J. S. Suh, I. Lee, K. Kim and S. W. Han, *Langmuir*, 2006, **22**, 1817.
- 38 J. Weber, Q. Su, M. Antonietti and A. Thomas, *Macromol. Rapid Commun.*, 2007, **28**, 1871.
- 39 B. Mu and K. S. Walton, *J. Phys. Chem. C*, 2011, **115**, 22748.
- 40 J.-P. Zhang, A.-X. Zhu, R.-B. Lin, X.-L. Qi and X.-M. Chen, *Adv. Mater.*, 2011, **23**, 1268.
- 41 H. Jasuja and K. S. Walton, *Dalton Trans.*, 2013, **42**, 15421.
- 42 N. C. Burtch, H. Jasuja and K. S. Walton, *Chem. Rev.*, 2014, **114**, 10575.
- 43 A. Samokhvalov, *Chem. – Eur. J.*, 2015, **21**, 16726.
- 44 P. Küsgens, M. Rose, I. Senkovska, H. Fröde, A. Henschel, S. Siegle and S. Kaskel, *Microporous Mesoporous Mater.*, 2009, **120**, 325.
- 45 J. Yan, Y. Yu, C. Ma, J. Xiao, Q. Xia, Y. Li and Z. Li, *Appl. Therm. Eng.*, 2015, **84**, 118.
- 46 X.-W. Liu, T.-J. Sun, J.-L. Hu and S.-D. Wang, *J. Mater. Chem. A*, 2016, **4**, 3584.
- 47 F. Jeremias, V. Lozan, S. K. Henninger and C. Janiak, *Dalton Trans.*, 2013, **42**, 15967.
- 48 H. Furukawa, F. Gándara, Y.-B. Zhang, J. Jiang, W. L. Queen, M. R. Hudson and O. M. Yaghi, *J. Am. Chem. Soc.*, 2014, **136**, 4369.
- 49 D. Fröhlich, S. K. Henninger and C. Janiak, *Dalton Trans.*, 2014, **43**, 15300.
- 50 V. Bon, N. Kavoosi, I. Senkovska and S. Kaskel, *ACS Appl. Mater. Interfaces*, 2015, **7**, 22292.
- 51 N. Al-Janabi, H. Deng, J. Borges, X. Liu, A. Garforth, F. R. Siperstein and X. Fan, *Ind. Eng. Chem. Res.*, 2016, **55**, 7941.